



Contrast-enhanced magnetic resonance imaging perfusion can predict microvascular invasion in patients with hepatocellular carcinoma (between 1 and 5 cm)

Lifang Wu¹ · Chun Yang² · Alice Halim³ · Shengxiang Rao² · Pengju Xu² · Wei Feng² · Caizhong Chen² · Yuan Ji⁴ · Jiayu Zhu⁵ · Mengsu Zeng²

Received: 13 October 2021 / Revised: 12 January 2022 / Accepted: 12 January 2022 / Published online: 3 February 2022
© The Author(s), under exclusive licence to Springer Science+Business Media, LLC, part of Springer Nature 2022

Abstract

Purpose To evaluate the role of perfusion parameters with MR imaging of the liver in diagnosing MVI in hepatocellular carcinoma (HCC) (between 1 and 5 cm).

Materials and methods This retrospective study was approved by the institutional review board. In 80 patients with 43 MVI(+) and 42 MVI(−) HCC, whole-liver perfusion MR imaging with Cartesian k-space undersampling and compressed sensing reconstruction was performed after injection of 0.1 mmol/kg gadopentetate dimeglumine. Parameters derived from a dual-input single-compartment model of arterial flow (Fa), portal venous flow (Fp), total blood flow (Ft = Fa + Fp), arterial fraction (ART), distribution volume (DV), and mean transit time (MTT) were measured. The significant parameters between the two groups were included to correlate with the presence of MVI at simple and multiple regression analysis.

Results In MVI-positive HCC, Fp was significantly higher than in MVI-negative HCC, whereas the reverse was seen for ART ($p < 0.001$). Tumor size ($\beta = 1.2, p = 0.004$; odds ratio, 3.20; 95% CI 1.45, 7.06), Fp ($\beta = 1.1, p = 0.004$; odds ratio, 3.09; 95% CI 1.42, 6.72), and ART ($\beta = -3.1, p = 0.001$; odds ratio, 12.13; 95% CI 2.85, 51.49) were independent risk factors for MVI. The AUC value of the combination of all three metrics was 0.931 (95% CI 0.855, 0.975), with sensitivity of 97.6% and specificity of 76.2%.

Conclusion The combination of Fp, ART, and tumor size demonstrated a higher diagnostic accuracy compared with each parameter used individually when evaluating MVI in HCC (between 1 and 5 cm).

Keywords Hepatocellular carcinoma · Prognosis · Pharmacokinetics · Magnetic resonance imaging

Lifang Wu and Chun Yang have contributed equally to this work.

✉ Mengsu Zeng
zeng.mengsu@zs-hospital.sh.cn

¹ Department of Radiology, Shanghai Institute of Medical Imaging, Zhongshan Hospital, Fudan University, No. 180, Fenglin Road, Xuhui 200032, Shanghai, China

² Department of Radiology, Zhongshan Hospital, Shanghai Institute of Medical Imaging, Fudan University, No. 180, Fenglin Road, Xuhui 200032, Shanghai, China

³ Shanghai Medical College, Fudan University, No. 138, Yixueyuan Road, Xuhui 200032, Shanghai, China

⁴ Department of Pathology, Zhongshan Hospital, Fudan University, No. 180, Fenglin Road, Xuhui 200032, Shanghai, China

⁵ Shanghai United Imaging Healthcare Co., Ltd. No. 2258, Chengbei Road, Jiading 201807, Shanghai, China

Introduction

Hepatocellular carcinoma (HCC) is the sixth most commonly diagnosed cancer worldwide and the fourth leading cause of cancer-related deaths [1]. Hepatic surgery is an appropriate choice for patients with early HCC, who have good liver function according to the European Association for Study of the Liver (EASL) and American Association for the Study of Liver Diseases (AASLD) guidelines [2, 3]. However, microvascular invasion (MVI) is a high risk factor for early recurrence during the first 2 years after hepatectomy [4, 5]. As such, the preoperative detection of the presence of MVI holds a significant clinical importance as it could help decrease the risk of reoccurrence by treatment with regional or systemic therapy to eradicate any microscopic foci in the liver remnant [6–9]. A major challenge at present is the absence of noninvasively diagnostic tools

to identify biologically aggressive features of the tumor. Several studies have reported that certain imaging findings including tumor size [10–12], peritumoral enhancement [5, 10], tumor margin [5, 10], and peritumoral hypointensity on gadoteric acid-enhanced hepatobiliary phase images [5, 13] were useful for predicting MVI in HCC. There is a definite trend in evaluating the presence of MVI in HCC using functional radiologic parameters [14, 15].

Radiologic findings about dynamic contrast-enhanced (DCE) MR imaging have only been examined in few studies to date. Golden-angle radial acquisition with compressed sensing reconstruction was reported for free-breathing dynamic liver imaging [16–18]. Liver perfusion imaging performed under breath-holding combined with shallow respiration is sensitive to respiratory motion and is limited by the extent of anatomical coverage that can be achieved [19–21]. Given the limitation, motion-free sequences such as LAVA-STAR [22] or GRASP VIBE [16, 18] were used for liver perfusion quantification. In addition, quantitative parameters derived from MR imaging are susceptible to artifacts such as B1 field inhomogeneity, and tissue T1 value is essential to convert signal intensity into contrast concentration for quantitative analysis [23, 24]. As such, a technique of DCE-MRI using Cartesian k-space undersampling with compressed sensing, which enables high temporal and adequate spatial resolution, was adopted in this study for whole-liver perfusion in free-breathing. Combined with T1 mapping and B1 inhomogeneity correction, we aimed to preoperatively identify MVI in HCC (between 1 and 5 cm) with MRI perfusion parameters.

Materials and methods

Patients

This retrospective clinical study was approved by our institutional review board. Between January 2018 and August 2018, a total of 132 consecutive patients underwent abdominal DCE MR imaging for focal liver lesion detection and characterization. The inclusion criteria were as follows: (1) a solitary tumor up to 5 cm in diameter or multiple tumors up to 3 in number and up to 3 cm in diameter for each tumor; (2) hepatectomy within 14 days after MR examinations; and (3) Child–Pugh class A/B [25]. The exclusion criteria were as follows: (1) lesions histopathologically diagnosed as tumors other than HCC; (2) small HCCs with diameters less than 1 cm; (3) presence of radiological evidence of macroscopic portal vein or hepatic vein invasion; (4) any prior recurrence of HCC; (5) history of prior therapy; (6) chronic renal dysfunction; (7) extrahepatic metastasis; and (8) poor MR image quality due to motion artifacts. Among these patients, 52 were excluded for the following reasons: 5 patients with

benign lesions, 1 patient with chronic kidney disease, seven patients with interventional therapy, 22 patients with non-HCC, 17 patients with unqualified DCE images. Finally, 80 patients (mean age, 56 years; range, 32–82 years) with 85 HCC, composed of 67 (83.8%) men (mean age, 56 years; range, 32–78 years) and 13 (16.2%) women (mean age, 58 years; range, 48–82 years) were included in this study. Of these HCC, 43 MVI-positive lesions and 42 MVI-negative lesions were identified on histology (Fig. 1).

Three Dimensional (3D) MR Imaging with Compressed Sensing for Hepatic Perfusion.

MR imaging was performed at a 3.0-T system with a torso phased-array coil (uMR 770, United Imaging Healthcare, Shanghai, China). All patients were asked to fast for 6 h before examination to avoid postprandial elevated portal venous flow [26]. Routine MRI was performed with the following sequence: axial T2-weighted single-shot fast spin echo sequence and T1-weighted dual-echo in-phase and opposed-phase gradient-echo sequence. A single-shot echo planar imaging sequence (b value of 0, 50, and 500 s mm⁻²) was used to obtain diffusion-weighted imaging (DWI). Subsequently, patients underwent successive whole-liver volumetric T1 and B1⁺ mappings prior to contrast injection. B1⁺ mapping was generated using the DREAM (Dual Refocusing Echo Acquisition Mode) technique, which was an ultra-fast multi-slice volumetric sequence [27]. T1 mapping was acquired using variable flip angle method, which was a 3D T1-weighted gradient-echo sequence with flip angles of 3°, 7°, 11°, and 15° [28]. Finally, followed by a

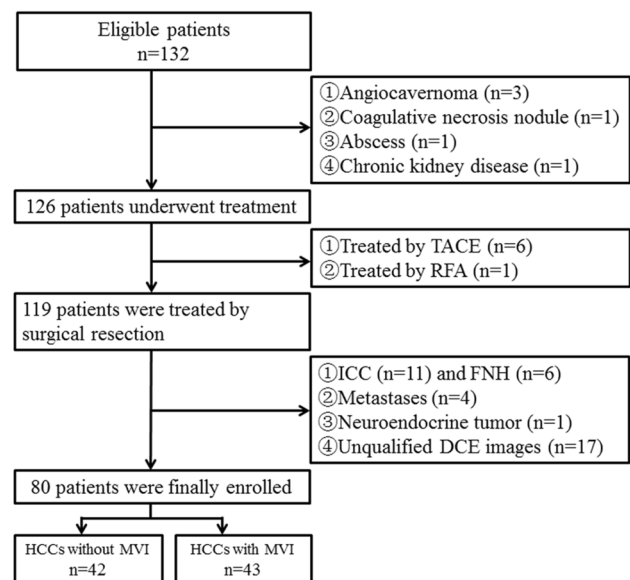


Fig. 1 Flow diagram of the study enrollment population. *TACE* transcatheter arterial chemoembolization, *RFA* radiofrequency ablation, *ICC* intrahepatic cholangiocarcinoma, *FNH* focal nodular hyperplasia, *DCE* dynamic contrast enhanced, *HCC* hepatocellular carcinoma, *MVI* microvascular invasion

whole-liver perfusion MR imaging with 3D spoiled gradient-echo (SPGRE) sequence in the axial plane. During 5–8 pre-contrast baseline acquisitions in free-breathing, a training procedure prior to the image data acquisition was adopted to learn patient's respiration pattern to determine an expiratory threshold. Only the image data corresponding to a position within the threshold were acquired with the help of a real-time feedback framework, which updated the respiration state and controlled the data acquisition. Next, 0.1 mmol/kg gadopentate dimeglumine ([Gd]) (Magnevist, Bayer Schering Pharma AG, Berlin, Germany) was injected, immediately followed by a 20-mL saline flush through a power injector at a rate of 4 mL/s. Another 40–43 phases of post contrast acquisitions were obtained within 3.2–3.5 min depending on the patient's respiration pattern with a temporal resolution up to 3.9–4.3 s/phase. More details (the protocol of perfusion MR imaging sequences and Cartesian k-space sampling) are available in the Supplementary Materials and Methods.

Image analysis

The images were transferred to workstation, uWS (United Imaging Healthcare, Shanghai, China), which runs a 4D-Analysis software package for image segmentation and coregistration. A square region of interest (ROI) was manually placed on the proximal abdominal aorta at the level of the celiac axis for arterial input function (AIF) calculation [29], which was used as an estimation for the hepatic arterial blood supply, another square was placed on the main portal vein at the level of the porta hepatis for the portal vein input function estimation (Fig. 2).

The conversion from signal intensity (SI) to Gd concentration was performed by inverting the non-linear relationship given by the SPGR signal equation [30], assuming a

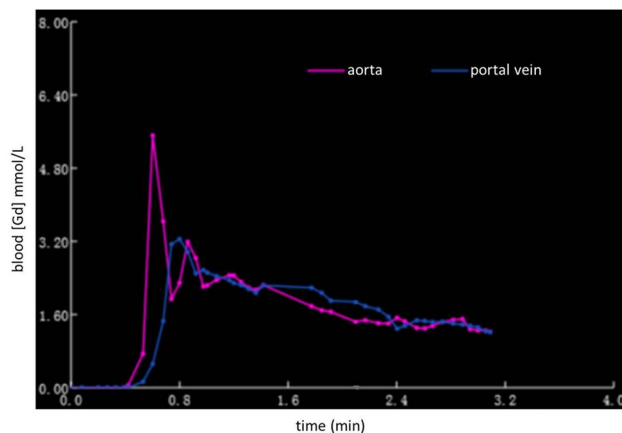


Fig. 2 Graph shows the concentration of gadopentate dimeglumine in the blood (abdominal aorta and portal vein) versus time curves for the aorta and portal vein

constant pre-contrast T1 value for blood at 1200 ms [31] and obtaining the T1 values for the tumor and liver parenchyma from the B1 inhomogeneity-corrected T1 map. Resulting time activity curves were fitted by using a dual-input single-compartment model:

$$\frac{dC_l(t)}{dt} = k_{1a} \cdot C_a(t) + k_{1p} \cdot C_p(t) - k_2 \cdot C_l(t)$$

where $C_a(t)$, $C_p(t)$, and $C_l(t)$ were the concentrations of contrast material in the aorta, portal vein, and liver, respectively; k_{1a} , k_{1p} and k_2 were constants for the aortic inflow rate, the portal venous inflow rate, and the outflow rate, respectively; t represented time and dt was the differential. All DCE images were used as the input for a voxel based curve fitting resulting in pseudocolor mappings of the hemodynamic parameters: arterial flow (F_a , ml/min/100 g), portal venous flow (F_p , ml/min/100 g), total blood flow ($F_t = F_a + F_p$, ml/min/100 g), arterial fraction ($ART = 100 \times F_a / F_t$, %), the distribution volume of Gd contrast through the liver compartment [$DV = 100 \times (k_{1a} + k_{1p}) / k_2$, %], and the average time it took a Gd molecule to traverse the liver from the arterial or portal inputs to the venous output given by the mean transit time ($MTT = 1/k_2$, s).

Measurements of tumor and liver parenchyma [tissue at more than 2 cm from the lesion [32] in the position far from heart and diaphragm] on all parametric maps of each patient were performed by an abdominal radiologist (L.F.W., with 6 years of experience) who was blinded to pathologic diagnosis. ROIs for tumor were manually delineated to include the whole tumor covering the largest axial-sectional area at enhanced phase, combined with adjacent upper and lower sections to obtain an average value. The ROIs were then transferred to the same regions on all parametric maps. When normal liver ROIs were drawn, care should be taken to avoid including any visible lesions, large vessels, artifacts, and the liver border, and the size were similar to that of the tumor.

Morphologic features evaluation

The conventional MR imaging features were assessed by one abdominal radiologist (S.X.R., with 20 years of experience), who was blinded to the results of MVI and DCE analysis. The following main potential features were evaluated: (a) presence and subclassification of single nodular smooth margin, focal extranodular growth, confluent multinodular growth, or infiltrative border with irregular shape via comprehensive analysis using T1-weighted, T2-weighted, and DCE imaging, respectively; (b) radiologic capsule appearance at delayed phase (180 s after injection of [Gd]), categorized as complete, incomplete, or absent; (c) peritumoral enhancement was assessed as detectable enhancing portion

adjacent to the tumor border (wedge-shaped type) or a larger range of enhancement surrounding the border (irregular circumferential type) at the arterial phase, turning isointense at the portal venous phase. The presence of hemorrhage, fat deposition, and necrosis were also assessed.

Histopathologic evaluation

Pathologic characteristics of each lesion were evaluated independently from surgical resection specimens, which were taken by a dedicated pathologist (Y.J., with 28 years of experience in hepatic pathology) who was unaware of the imaging results. Histologically, MVI was defined as a tumor within a vascular space lined by endothelium that was visible only at microscopy.

Statistical analysis

The sample size was determined by using power analysis according to our pretest values of sensitivity of 0.9 and specificity of 0.8 for each hemodynamic parameter by presuming an incidence rate of MVI in HCC (between 1 and 5 cm) of 0.35 [5], an α value of 0.05, and a power of 0.9, yielding an expected sample size of 42. Student's *t* test or Mann–Whitney *U* test was used for continuous variables depending on their distribution and Pearson's chi-squared test or Fisher's exact test was used for categorical variables. Univariate and multivariate logistic regression analyses were performed to screen the independent risk factors of MVI. Factors with a *P* value of 0.05 or less at univariate analyses were entered into a stepwise logistic regression model (conditional backward elimination) to assess for the best predictor of MVI [33]. The absence of multicollinearity was ensured by calculating the variance inflation factor (VIF) less than 10 in the model. The standardized coefficients called β weights and coefficients of determination (R^2) were reported as descriptors of the model [33]. Receiver operating characteristic (ROC) curve analyses were performed to evaluate the diagnostic performance. Areas under the curves (AUCs) were compared using the DeLong method. A difference with a *P* value of less than 0.05 was considered statistically significant. Statistical analyses were performed by using SPSS (v. 20.0, Chicago, IL) and MedCalc (MedCalc, Mariakerke, Belgium).

Results

Clinical-pathologic characteristics

The pretreatment characteristics of all patients are presented in Table 1. Seventy-five patients had solitary HCC between 1 and 5 cm in diameter, and the remaining five had two lesions between 1 and 3 cm in diameter, respectively, among which one had a MVI-negative lesion and the rest had two MVI-negative lesions. Apart from variations in BCLC stage and tumor size, other baseline clinical-pathologic characteristics showed no significant differences between the MVI-positive and MVI-negative groups of the study populations. The number of patients at BCLC stage 0 was higher in MVI-negative group than that in MVI-positive group (13/37, 35.1% vs 4/43, 9.3%; $P=0.011$), and tumor size of HCC with MVI was larger than that of HCC without MVI (mean \pm SD, 3.56 ± 1.04 cm [range, 1.4–5.0] vs 2.58 ± 1.23 cm [range, 1.2–5.0]; $P<0.001$).

Conventional MR imaging findings

According to the lesion's morphologic features in MR imaging, its radiological capsule integrity, peritumoral enhancement, as well as presence of hemorrhage, fat deposition, and necrosis revealed no significant difference between the MVI-positive and MVI-negative groups, except for tumor margin ($P=0.032$) (Table 2). Focal extranodular growth significantly appeared more frequently in HCC with MVI compared to those without MVI (10/43, 23.3% vs 1/42, 2.4%; $P=0.017$), whereas confluent multinodular growth and infiltrative border with irregular shape showed no significant difference between the two groups based on the reference of smooth margin (3/43, 7.0% vs 2/42, 4.8%, $P=0.475$; 1/43, 2.3% vs 1/42, 2.4%, $P=0.851$).

Perfusion parameters

In both groups, the Fa, ART, and DV were significantly higher in HCC than in normal liver parenchyma, while Fp was significantly lower in HCC than in normal liver parenchyma (Table 3; $P<0.001$).

Table 1 Patient baseline characteristics

Parameter	All	MVI-positive	MVI-negative	<i>P</i> Value
Age (years), mean \pm SD	56 \pm 10	55 \pm 10	58 \pm 9	.208
Male/female (n)	67/13	36/7	31/6	1.0
Hepatitis B virus, Y/N	70/10	37/6	33/4	.745
Antiviral treatment, Y/N	31/39	14/23	17/16	.335
Child–Pugh A/B (n)	80/0	43/0	37/0	
BCLC stage 0/A/B (n)	17/63/0	4/39/0	13/24/0	.011
Pretreatment laboratory markers				
ALT > 50 U/L, Y/N	17/63	10/33	7/30	.785
AST > 40 U/L, Y/N	19/61	10/33	9/28	1.0
ALP > 125 U/L, Y/N	9/71	2/41	7/30	.073
GGT > 60 U/L, Y/N	24/56	14/29	10/27	.632
INR > 1.2, Y/N	5/75	3/40	2/35	1.0
Total bilirubin > 0.336 mg/dL, Y/N	20/60	11/32	9/28	1.0
Albumin < 35 g/L, Y/N	1/79	0/43	1/36	.462
Creatinine > 1.5 mg/dL, Y/N	2/78	2/41	0/37	.496
AFP > 20 ng/mL, Y/N	41/39	26/17	15/22	.115
Tumor				
Number of HCC	85	43	42	.180
One	75	42	33	
Two	5	1	4	
Tumor size (cm), Mean \pm SD	3.08 \pm 1.23	3.56 \pm 1.04	2.58 \pm 1.23	< .001
Lesion distribution				
Unilobar (L/R/C)	74(22/51/1)	34(9/25/0)	40(13/26/1)	.102
Bilobar	11	9	2	
Pathologic findings				
Edmondson–Steiner grade				.676
G1–G2	80	41	39	
G3–G4	5	2	3	
Fibrosis stage				
S0	4	3	1	.574
S1–S2	17	9	8	
S3–S4	64	31	33	

ALT alanine aminotransferase; AST aspartate aminotransferase; ALP alkaline phosphatase; GGT gamma-glutamyl transpeptidase; INR international normalized ratio; AFP alpha fetoprotein; SD standard deviation; L left lobe; R right lobe; C caudate lobe; Y yes; N no. Tumor size was compared using a Mann–Whitney *U* test. Numbers for the rest of parameters were compared for significance using Pearson's chi-squared test or Fisher's exact test

Comparing the perfusion parameters between the two groups, Fp was significantly higher in the MVI-positive HCC than in the MVI-negative HCC, whereas this finding was reversed for ART ($P < 0.001$). MTT was significantly higher in the MVI-negative HCC than in the MVI-positive HCC ($P = 0.019$). No significant difference was observed for Fa ($P = 0.866$), Ft ($P = 0.064$), and DV ($P = 0.206$) between MVI-positive and MVI-negative groups (Fig. 3).

Risk factors for MVI of HCC

In terms of significant morphologic features and quantitative parameters derived from DCE, Table 4 showed the risk factors that were found to be significantly related to MVI in HCC (between 1 and 5 cm) at univariate analysis: presence of focal extranodular growth with the reference category of smooth margin ($\beta = 1.2$, $P = 0.017$, $R^2 = 0.16$), increased

Table 2 Analysis of radiologic features for the relationship with MVI of 85 HCCs

Parameter	No. of lesions <i>n</i> =85	MVI-positive <i>n</i> =43	MVI-negative <i>n</i> =42	<i>P</i> Value
Tumor margin				.032
Smooth	67 (78.8)	29 (67.4)	38 (90.5)	
Focal extranodular growth	11 (12.9)	10 (23.3)	1 (2.4)	
Confluent multinodular growth	5 (5.9)	3 (7.0)	2 (4.8)	
Infiltrative border with irregular shape	2 (2.4)	1 (2.3)	1 (2.4)	
Radiologic capsule integrity				.446
Complete	25 (29.4)	10 (23.3)	15 (35.7)	
Incomplete	45 (52.9)	25 (58.1)	20 (47.6)	
Absent	15 (17.6)	8 (18.6)	7 (16.7)	
Peritumoral enhancement				.350
Absent	74 (87.1)	37 (86.0)	37 (88.1)	
Wedge shaped	9 (10.6)	4 (9.3)	5 (11.9)	
Irregular circumferential	2 (2.4)	2 (4.7)	0	
Hemorrhage				.227
Absent	72 (84.7)	34 (79.1)	38 (90.5)	
Present	13 (15.3)	9 (20.9)	4 (9.5)	
Fat deposition				.712
Absent	77 (90.6)	38 (88.4)	39 (92.9)	
Present	8 (9.4)	5 (11.6)	3 (7.1)	
Necrosis				.494
Absent	83 (97.6)	41 (95.3)	42 (100.0)	
Present	2 (2.4)	2 (4.7)	0	

Data are numbers of lesions, with percentages in parentheses. Data are compared by using Pearson's chi-squared test or Fisher's exact test

tumor size ($\beta=0.8$, $P<0.001$, $R^2=0.21$), Fp ($\beta=1.2$, $P<0.001$, $R^2=0.31$) value, and decreased ART ($\beta=-2.5$, $P<0.001$, $R^2=0.51$), and MTT ($\beta=-0.6$, $P=0.022$, $R^2=0.07$). In multiple regression analysis, all candidate variables showing significant association at univariate analysis were included at the start, the VIF of the multiple regression models ranged from 1.09 to 1.53. With the deletion of insignificant variables step by step, tumor size ($\beta=1.2$, $P=0.004$; odds ratio, 3.20; 95% CI 1.45, 7.06), Fp ($\beta=1.1$, $P=0.004$; odds ratio, 3.09; 95% CI 1.42, 6.72), and ART ($\beta=-2.5$, $P=0.001$; odds ratio, 12.13; 95% CI: 2.85, 51.49) were independent risk factors for MVI (Fig. 4). The R^2 value for the goodness-of-fit test of the multiple regression model was 0.719. ROC curves of ART, Fp, and tumor size and their combinations for predicting MVI are plotted in Fig. 5. The optimal cutoff value, as well as corresponding AUC, *P* value, sensitivity, specificity, positive predictive value (PPV), and negative predictive value (NPV) are presented in Table 5. The AUC values of ART, Fp, and tumor size were 0.861

(95% CI 0.769, 0.927), 0.791 (95% CI 0.689, 0.871), and 0.733 (95% CI 0.626, 0.823), respectively. For pairwise comparisons of ROC curves, there were no significant differences among ART, Fp and tumor size in diagnosing MVI ($P=0.060$ – 0.448). The AUC value of the combination of all three metrics was 0.931 (95% CI: 0.855, 0.975), which was significantly superior than the performance of ART, Fp and tumor size used alone ($P<0.05$), with a sensitivity of 97.6%, specificity of 76.2%, PPV of 80.8%, and NPV of 97.0%.

Discussion

The study initially evaluated the differences of MRI perfusion parameters derived from dual-input single-compartment model between HCC and peripheral liver parenchyma, and between MVI-positive and MVI-negative HCC lesions. The results suggested that the increased Fp, the decreased ART, and tumor size ≥ 2.5 cm in diameter were independently correlated with MVI in HCC (between 1 and 5 cm), and

Table 3 Analysis of DCE-MRI parameters of HCC and normal liver parenchyma between MVI-positive and MVI-negative groups

Parameter		MVI-positive	MVI-negative	<i>P</i> *Value
Fa (ml/min/100 g)	HCC	57.34 ± 24.78	58.17 ± 20.45	.866
	Liver	23.43 ± 10.40	24.03 ± 68.25	.754
	<i>P</i> † value	<.001	<.001	
Fp (ml/min/100 g)	HCC	36.58 ± 13.32	22.34 ± 12.85	<.001
	Liver	63.37 ± 25.09	60.08 ± 23.11	.471
	<i>P</i> † value	<.001	<.001	
Ft (ml/min/100 g)	HCC	93.91 ± 36.56	80.51 ± 31.38	.064
	Liver	86.80 ± 32.70	84.11 ± 26.68	.648
	<i>P</i> † value	.336	.348	
ART (%)	HCC	57.71 ± 9.43	71.41 ± 9.39	<.001
	Liver	31.09 ± 7.42	29.15 ± 7.51	.234
	<i>P</i> † value	<.001	<.001	
MTT (sec)	HCC	18.3 ± 9.2	24.1 ± 12.1	.019
	Liver	16.9 ± 4.6	18.1 ± 5.9	.629
	<i>P</i> † value	.976	.009	
DV (%)	HCC	24.65 ± 7.17	27.94 ± 10.54	.206
	Liver	19.49 ± 10.64	19.22 ± 4.94	.426
	<i>P</i> † value	<.001	<.001	

Data are means ± standard deviation. *Fa* arterial blood flow; *Fp* portal venous blood flow; *Ft* total blood flow; *ART* arterial fraction; *MTT* mean transit time; *DV* distribution volume. Between the MVI-positive and MVI-negative groups, the difference of *Fa*, *Fp*, and *ART* of HCC, and the difference of *Fa* of normal liver parenchyma were compared for significance using a Student's *t* test; Numbers for the rest of parameters were compared using a Mann–Whitney *U* test. Between HCC and normal liver parenchyma, the difference of *Fp* in MVI-positive group, and the difference of *Ft* in MVI-negative group were compared for significance using a Student's *t* test; Numbers for the rest of parameters were compared using a Mann–Whitney *U* test

*The difference of parameters between the MVI-positive and MVI-negative groups

†The difference of parameters between HCC and normal liver parenchyma

that the combination of all three parameters showed higher diagnostic accuracy compared with each used individually.

Several studies have investigated the application of dynamic contrast-enhanced image for perfusion quantification of HCC and liver parenchyma. Taouli et al. [34] used a dual-input single-compartment model to quantify MRI perfusion parameters in patients with HCC. They demonstrated higher *Fa* and *ART* and lower *Fp* in HCC compared with hepatic parenchyma, findings not similar to ours were *DV* and *MTT*, where they reported lower *DV* in HCC and no difference of *MTT* between HCC and surrounding liver. Wu et al. [15] also found higher hepatic artery flow (HAF), perfusion index (equivalent to *ART*) and lower portal vein flow (PVF) in HCC than in normal hepatic parenchyma using a dual-input maximum slope analysis method with

dynamic CT. Besides, they presented the similar change in HAF, PVF, and total flow of small HCC (≤ 3 cm) between MVI (+) and MVI (–) groups as observed in our study. The arterial and portal vein flow related parameters were logically supposed to be more robust ones. In theory, the step-wise hepatocarcinogenesis is associated with a progression toward increasing in arterial blood flow and decreasing in portal venous flow [35–37]. In HCC with MVI, the observed increase in *Fp* might be caused by the effect of high permeability, and hepatic artery-portal vein fistula formation, with subsequent decrease of the *ART*. Unlike in previous studies involving quantitative MR perfusion imaging, in the present study, 3D data encompassing the entire liver were acquired. This had an additional advantage of enabling measurement of a vascular input function close to the tissue.

New sequences combining Cartesian k-space undersampling with compressed sensing reconstruction enable high accelerations in dynamic liver imaging with a temporal resolution up to 3.9–4.3 s/phase to catch the peak concentration of AIF, while maintaining an acceptable level of signal to noise ratio (SNR) and adequate spatial resolution for anatomic visualization [38]. Golden-angle radial acquisition with compressed sensing reconstruction was reported for free-breathing dynamic liver imaging [16–18]. However, compared to Cartesian sampling, the time efficiency of k-space coverage in radial trajectories is much lower, especially when combined with square in-plane FOV and restricted sampling along slice dimension in stack-of-stars acquisition. Even though Cartesian sequences were motion-sensitive, in the presented sequence, we used gating approaches in free-breathing to ensure that data were always acquired at the end expiratory phase, which mitigates respiratory motion effects as much as possible. Hausmann et al. [39] demonstrated that compressed sensing free-breathing VIBE using motion-state-resolved reconstructions, and an echo train assigned as the sixth movement state, was technically feasible with improved image quality compared to the breath-hold VIBE. There was following potential risk of data undersampling within some temporal periods, resulting in sub-optimal characterization of the peak arterial enhancement and consequently the AIF. The strategy to mitigate this was to choose the reconstructed AIF curves of better quality, which presented a steep upslope, a high concentration first pass peak and a steep downslope, followed by a small recirculation peak based on the previous research [40]. In addition, bias due to field inhomogeneity was avoided to a large extent with B1 correction, and the T1 relaxation time based indices of the whole liver were more reliable [23]. In this sense, our method provides a solid base for an accurate whole-liver perfusion analysis and a reliable pharmacokinetic parameter evaluation.

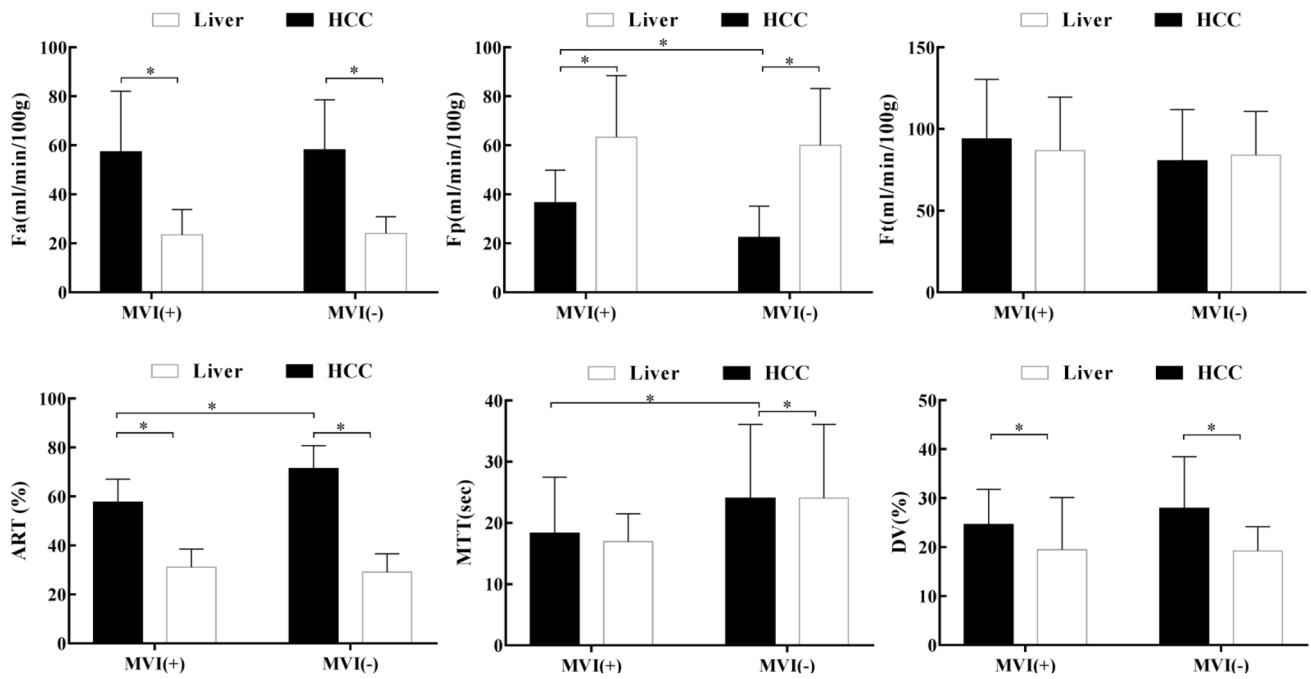


Fig. 3 Comparison of perfusion parameters between the MVI-positive HCC and the MVI-negative HCC and between HCC and liver parenchyma in both groups. *The difference of parameters was significant. *MVI* microvascular invasion, *HCC* hepatocellular carcinoma

Table 4 Univariate and multivariate analyses of risk factors for MVI of HCC (between 1 and 5 cm)

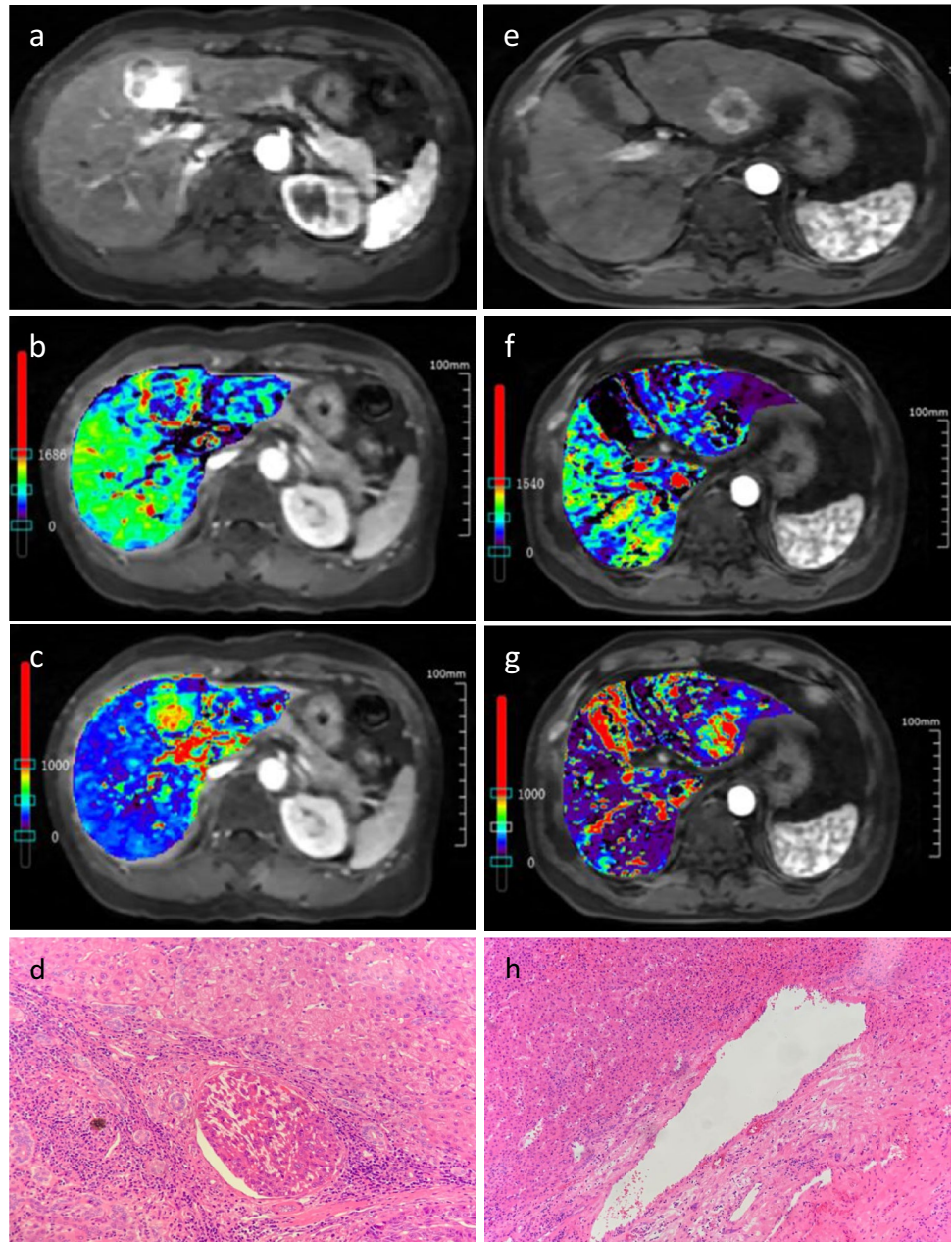
Risk Factor	Univariate analysis				Multivariate analysis		
	R ² Value	β Value	Odds ratio	P Value	β Value	Odds ratio	P Value
Tumor size	0.21	0.8	2.43(1.47,4.02)	<.001	1.2	3.20 (1.45,7.06)	.004
Nonsmooth tumor margin							
Smooth*							
Focal extranodular growth	0.16	1.2	3.62 (1.25,10.40)	.017			.113
Confluent multinodular growth	0.01	0.6	1.96 (0.30,12.54)	.475			
Infiltrative border with irregular shape		0.1	1.09 (0.42,2.79)	.851			
Fp (ml/min/100 g)	0.31	1.2	3.39 (1.85,6.19)	<.001	1.1	3.09 (1.42, 6.72)	.004
ART (%)	0.51	- 2.5	12.32 (3.75,40.48)	<.001	-2.5	12.13(2.85,51.49)	.001
MTT (sec)	0.07	- 0.6	0.55 (0.33,0.92)	.022			.562

Data in parentheses are 95% CIs

Fp portal venous blood flow; *ART* arterial fraction; *MTT* mean transit time

*Data were used as the reference category

Fig. 4 **a** MVI (+) HCC in a 60-year-old female patient in the left lobe (segments 4). MVI(+) HCC shows a higher Fp (**b** blue color in the lesion) and a lower ART (**c** green color in the lesion). **d** Microscopy (hematoxylin–eosin stain, $\times 20$) shows a cluster of carcinoma cells in microvessel. **e** MVI (–) HCC in a 61-year-old male patient in the left lobe (segments 2). MVI(-) HCC shows a lower Fp (**f** black color in the lesion) and a higher ART (**g** red color in the lesion). **h** Microscopy (hematoxylin–eosin stain, $\times 10$) shows no carcinoma cells in microvessel. *MVI* microvascular invasion, *HCC* hepatocellular carcinoma, *Fp* portal venous flow, *ART* arterial fraction



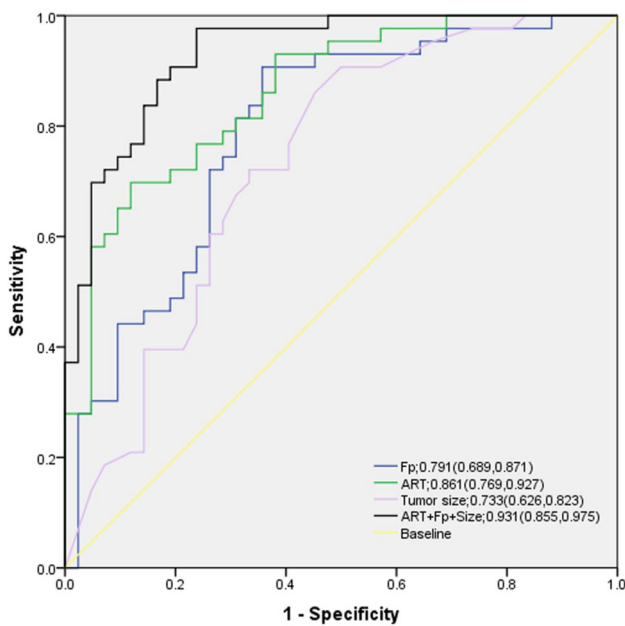


Fig. 5 Receiver operating characteristic (ROC) curve and corresponding areas under ROC curve (AUCs) of significant parameters for prediction of MVI. Numbers in parentheses represent 95% confidence intervals. *MVI* microvascular invasion

as incomplete radiologic capsule, irregular circumferential enhancement, and size were also reported to be related to MVI of HCC [42, 43]. These results of the different studies were inconsistent in varying degrees. Selection bias of surgical candidates might be the cause of disagreements among different studies.

There were a number of limitations in this study. Firstly, imaging technique repeatability of the free-breathing MR perfusion for liver was not performed; however, the comprehensive details in acquisition techniques and MR parameters made the experiment reproducible. Secondly, despite the whole-liver perfusion imaging with compressed sensing allowed high temporal resolution for the perfusion parameters estimation, the compromised spatial resolution was still difficult for the small lesions (< 1 cm) detection. Thus, we excluded small HCCs less than 1 cm in diameter.

In conclusion, free-breathing 3D MR imaging with compressed sensing reconstruction for whole-liver perfusion provides an excellent approach to quantitatively evaluate MVI in HCC (between 1 and 5 cm). When coupled with the Fp, ART, and tumor size, higher diagnostic accuracy can be obtained than each parameter used individually.

Table 5 ART, Kep, and tumor size results for prediction of MVI in HCC (between 1 and 5 cm)

Variables	Sensitivity	Specificity	PPV	NPV	Cutoff value	AUC	P Value
ART (%)	69.7	88.1	85.7	74.0	62.5	0.861 (0.769,0.927)	<.001
Fp (ml/min/100 g)	90.7	64.3	72.2	87.1	22.33	0.791 (0.689,0.871)	<.001
Tumor size	86.1	54.7	66.1	79.3	2.40	0.733 (0.626,0.823)	<.001
ART+Fp+Size	97.6	76.2	80.8	97.0		0.931 (0.855,0.975)	<.001

Data in parentheses are 95% CIs

PPV positive predictive value; NPV negative predictive value; AUC area under the ROC curve; ART arterial fraction; Fp portal venous blood flow

Previous studies [5, 41] reported that imaging feature of non-smooth tumor margin in HCC was independently associated with MVI, and several potential risk factors such

Supplementary information The online version contains supplementary material available at <https://doi.org/10.1007/s00261-022-03423-6>.

Acknowledgements This work received funding from 1. National Natural Science Foundation of China (Grant Number 91859107) and 2. Shanghai Science and Technology Committee (Grant Number 18DZ1930102).

References

- Bray F, Ferlay J, Soerjomataram I, Siegel RL, Torre LA, Jemal A. Global cancer statistics 2018: GLOBOCAN estimates of incidence and mortality worldwide for 36 cancers in 185 countries. *CA Cancer J Clin* 2018;68:394–424.
- European Association for the Study of the Liver. EASL-EORTC clinical practice guidelines: management of hepatocellular carcinoma. *J Hepatol* 2012; 56:908–943. <https://doi.org/10.1016/j.jhep.2011.12.001>.
- Bruix J, Sherman M. Management of hepatocellular carcinoma. *Hepatology* 2005; 42:1208–1236.
- Kluger MD, Salceda JA. et al. Liver resection for hepatocellular carcinoma in 313 Western patients: tumor biology and underlying liver rather than tumor size drive prognosis. *J Hepatol* 2015; 62:1131–1140.
- Lee S, Kim SH, Lee JE, Sinn DH, Park CK. Preoperative gadoteric acid-enhanced MRI for predicting microvascular invasion in patients with single hepatocellular carcinoma. *J Hepatol* 2017; 67:526–534.
- Dhir M, Melin AA. et al. A Review and Update of Treatment Options and Controversies in the Management of Hepatocellular Carcinoma. *Ann Surg* 2016; 263:1112–1125.
- Cillo U, Vitale A, Polacco M, Fasolo E. Liver transplantation for hepatocellular carcinoma through the lens of transplant benefit. *Hepatology* 2017; 65:1741–1748.
- Qi YP, Zhong JH. et al. Adjuvant transarterial chemoembolization for patients with hepatocellular carcinoma involving microvascular invasion. *Am J Surg* 2019; 217:739–744.
- Wang Z, Ren Z. et al. Adjuvant Transarterial Chemoembolization for HBV-Related Hepatocellular Carcinoma After Resection: A Randomized Controlled Study. *Clin Cancer Res* 2018; 24:2074–2081.
- Renzulli M, Buonfiglioli F. et al. Imaging features of microvascular invasion in hepatocellular carcinoma developed after direct-acting antiviral therapy in HCV-related cirrhosis. *Eur Radiol* 2018; 28:506–513.
- Kim MJ, Lee M, Choi JY, Park YN. Imaging features of small hepatocellular carcinomas with microvascular invasion on gadoteric acid-enhanced MR imaging. *Eur J Radiol* 2012; 81:2507–2512.
- Zhou Y, Wang X. et al. Mass-forming intrahepatic cholangiocarcinoma: Can diffusion-weighted imaging predict microvascular invasion? *J Magn Reson Imaging* 2019; 50:315–324.
- Kim KA, Kim MJ. et al. Prediction of microvascular invasion of hepatocellular carcinoma: usefulness of peritumoral hypointensity seen on gadoteric acid-enhanced hepatobiliary phase images. *J Magn Reson Imaging* 2012; 35:629–634.
- Wang WT, Yang L. et al. Assessment of Microvascular Invasion of Hepatocellular Carcinoma with Diffusion Kurtosis Imaging. *Radiology* 2018; 286:571–580.
- Wu D, Tan M. et al. Liver computed tomographic perfusion in the assessment of microvascular invasion in patients with small hepatocellular carcinoma. *Invest Radiol* 2015; 50:188–194.
- Feng L, Axel L, Chandarana H, Block KT, Sodickson DK, Otazo R. XD-GRASP: Golden-angle radial MRI with reconstruction of extra motion-state dimensions using compressed sensing. *Magn Reson Med* 2016; 75:775–788.
- Chandarana H, Feng L. et al. Respiratory Motion-Resolved Compressed Sensing Reconstruction of Free-Breathing Radial Acquisition for Dynamic Liver Magnetic Resonance Imaging. *Invest Radiol* 2015; 50:749–756.
- Chandarana H, Feng L. et al. Free-breathing contrast-enhanced multiphase MRI of the liver using a combination of compressed sensing, parallel imaging, and golden-angle radial sampling. *Invest Radiol* 2013; 48:10–16.
- Hagiwara M, Rusinek H. et al. Advanced liver fibrosis: diagnosis with 3D whole-liver perfusion MR imaging--initial experience. *Radiology* 2008; 246:926–934.
- Coenegrachts K, Bols A, Haspelslagh M, Rigauts H. Prediction and monitoring of treatment effect using T1-weighted dynamic contrast-enhanced magnetic resonance imaging in colorectal liver metastases: potential of whole tumour ROI and selective ROI analysis. *Eur J Radiol* 2012; 81:3870–3876.
- Annet L, Materne R, Danse E, Jamart J, Horsmans Y, Van Beers BE. Hepatic flow parameters measured with MR imaging and Doppler US: correlations with degree of cirrhosis and portal hypertension. *Radiology* 2003; 229:409–414.
- Jahng GH, Li KL, Ostergaard L, Calamante F. Perfusion magnetic resonance imaging: a comprehensive update on principles and techniques. *Korean J Radiol* 2014; 15:554–577.
- Yoon JH, Lee JM, Kim E, Okuaki T, Han JK. Quantitative Liver Function Analysis: Volumetric T1 Mapping with Fast Multislice B1 Inhomogeneity Correction in Hepatocyte-specific Contrast-enhanced Liver MR Imaging. *Radiology* 2017; 282:408–417.
- Bergamino M, Bonzano L, Levrero F, Mancardi GL, Roccatagliata L. A review of technical aspects of T1-weighted dynamic contrast-enhanced magnetic resonance imaging (DCE-MRI) in human brain tumors. *Phys Med* 2014; 30:635–643.
- Lim KC, Chow PK, Allen JC, Siddiqui FJ, Chan ES, Tan SB. Systematic review of outcomes of liver resection for early hepatocellular carcinoma within the Milan criteria. *Br J Surg* 2012; 99:1622–1629.
- Gaiani S, Bolondi L, Li BS, Santi V, Zironi G, Barbara L. Effect of meal on portal hemodynamics in healthy humans and in patients with chronic liver disease. *Hepatology* 1989; 9:815–819.
- Sprinkart AM, Nehrke K. et al. Ultrafast volumetric B1 (+) mapping for improved radiofrequency shimming in 3 tesla body MRI. *J Magn Reson Imaging* 2014; 40:857–863.
- Deoni SC, Rutt BK, Peters TM. Rapid combined T1 and T2 mapping using gradient recalled acquisition in the steady state. *Magn Reson Med* 2003; 49:515–526.
- Buckley DL, Roberts C, Parker GJ, Logue JP, Hutchinson CE. Prostate cancer: evaluation of vascular characteristics with dynamic contrast-enhanced T1-weighted MR imaging--initial experience. *Radiology* 2004; 233:709–715.
- Aronhime S, Calcagno C. et al. DCE-MRI of the liver: effect of linear and nonlinear conversions on hepatic perfusion quantification and reproducibility. *J Magn Reson Imaging* 2014; 40:90–98.
- Bentzen L, Vestergaard-Poulsen P. et al. Intravascular contrast agent-enhanced MRI measuring contrast clearance and tumor blood volume and the effects of vascular modifiers in an experimental tumor. *Int J Radiat Oncol Biol Phys* 2005; 61:1208–1215.
- Lu Q, Ling W. et al. Hepatocellular carcinoma: stiffness value and ratio to discriminate malignant from benign focal liver lesions. *Radiology* 2015; 275:880–888.
- Leitao HS, Doblaz S. et al. Hepatic Fibrosis, Inflammation, and Steatosis: Influence on the MR Viscoelastic and Diffusion Parameters in Patients with Chronic Liver Disease. *Radiology* 2017; 283:98–107.
- Taouli B, Johnson RS. et al. Hepatocellular carcinoma: perfusion quantification with dynamic contrast-enhanced MRI. *AJR Am J Roentgenol* 2013; 201:795–800.

35. Roncalli M, Roz E. et al. The vascular profile of regenerative and dysplastic nodules of the cirrhotic liver: implications for diagnosis and classification. *Hepatology* 1999; 30:1174–1178.
36. Park YN, Yang CP, Fernandez GJ, Cubukcu O, Thung SN, Theise ND. Neovascularization and sinusoidal "capillarization" in dysplastic nodules of the liver. *Am J Surg Pathol* 1998; 22:656–662.
37. Efremidis SC, Hytiroglou P. The multistep process of hepatocarcinogenesis in cirrhosis with imaging correlation. *Eur Radiol* 2002; 12:753–764.
38. Khalifa F, Soliman A. et al. Models and methods for analyzing DCE-MRI: a review. *Med Phys* 2014; 41:124301.
39. Hausmann D, Niemann T. et al. Free-Breathing Dynamic Contrast-Enhanced Imaging of the Upper Abdomen Using a Cartesian Compressed-Sensing Sequence With Hard-Gated and Motion-State-Resolved Reconstruction. *Invest Radiol* 2019; 54:728–736.
40. Parker GJ, Roberts C. et al. Experimentally-derived functional form for a population-averaged high-temporal-resolution arterial input function for dynamic contrast-enhanced MRI. *Magn Reson Med* 2006; 56:993–1000.
41. Huang M, Liao B. et al. Prediction of Microvascular Invasion in Hepatocellular Carcinoma: Preoperative Gd-EOB-DTPA-Dynamic Enhanced MRI and Histopathological Correlation. *Contrast Media Mol Imaging* 2018; 2018:9674565.
42. Lv J, Yin H, Mao W, Shi H. Investigating the value of pre-treatment (18)F-FDG PET/CT in predicting the pathological characteristic of hepatocellular carcinoma and recurrence after liver transplantation. *Abdom Radiol* 2021;46:2490–2497.
43. Song Q, Guo Y. et al. Comparative study of evaluating the micro-circulatory function status of primary small HCC between the CE (DCE-MRI) and Non-CE (IVIM-DWI) MR Perfusion Imaging. *Abdom Radiol* 2021;46:2575–2583.

Publisher's Note Springer Nature remains neutral with regard to jurisdictional claims in published maps and institutional affiliations.